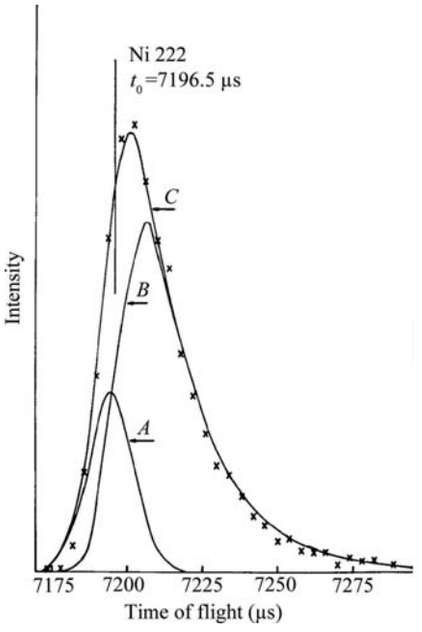

Figure 3.3.3
The observed and calculated Ni 222 diffraction line profile from the Back Scattering Spectrometer, Harwell Laboratory, Chilton, UK. The curves *A* and *B* are computed from the two terms in equation (3.3.19) and curve *C* is the sum (from Von Dreele *et al.*, 1982).

particularly for long-pulse sources, to give what is seen at the powder diffractometer.

Consequently, the neutron pulse structure from these sources has a complex and asymmetric shape, usually characterized by a very sharp rise and a slower decay, both of which are dependent on the neutron wavelength. The resulting powder diffraction peak profile (Fig. 3.3.3) is then the convolution [equation (3.3.2)] of this pulse shape (G_λ) with symmetric functions (G_I) arising from beamline components (*e.g.* slits and choppers) and the sample characteristics (G_S).

3.3.3.3. *The neutron TOF powder peak profile*

An early attempt at representing the TOF peak profile used a piecewise approach combining a leading-edge Gaussian, a peak-top Gaussian and an exponential decay for the tail (Cole & Windsor, 1980). Although single peaks could be fitted well with this function, the variation with TOF was complex and required many arbitrary coefficients.

A more successful approach empirically represented the pulse shape by a pair of back-to-back exponentials which were then convoluted with a Gaussian (Jorgensen *et al.*, 1978; Von Dreele *et al.*, 1982) to give

$$P(\Delta) = \frac{\alpha\beta}{\alpha+\beta}\left\{\exp\left[\frac{\alpha}{2}(\alpha\sigma^2+2\Delta)\right]\operatorname{erfc}\left[\frac{\alpha\sigma^2+\Delta}{\sigma(2^{1/2})}\right] + \exp\left[\frac{\beta}{2}(\beta\sigma^2-2\Delta)\right]\operatorname{erfc}\left[\frac{\beta\sigma^2-\Delta}{\sigma(2^{1/2})}\right]\right\}, \tag{3.3.19}$$

where α and β are, respectively, the coefficients for the exponential rise and decay functions; erfc is the complementary error function. Analysis of the data that were available then gave empirical relations for α, β and σ as

$$\alpha = \alpha_1/d; \quad \beta = \beta_0 + (\beta_1/d^4); \quad \sigma = \sigma_1 d. \tag{3.3.20}$$

The two terms in this function are shown in Fig. 3.3.3. The junction of the two exponentials defines the peak position (shown as a vertical line in Fig. 3.3.3); it is offset to the low side of the peak maximum. This arbitrary choice of peak position then affects the relationship between the TOF and reflection *d*-spacing; an empirical relationship (Von Dreele *et al.*, 1982) was found to suffice:

$$\mathrm{TOF} = Cd + Ad^2 + Z, \tag{3.3.21}$$

with three adjustable coefficients (C, A, Z) established *via* fitting to the pattern from a standard reference material.

Although this profile description was adequate for room-temperature moderators (H_2O or polyethylene) at low-power spallation sources, it does not describe well the wavelength dependence for cold moderators feeding neutron guides used at higher-power sources. An alternative description, employing a switch function to account for the fundamental change in the neutron leakage profile from the moderator between epithermal and thermal neutrons, was proposed (Ikeda & Carpenter, 1985; Robinson & Carpenter, 1990) to accommodate the profiles seen from liquid CH_4 or H_2 moderators. A drawback of this description is that the pulse profile is defined with the peak position at the low TOF edge; convolution with G_I and G_S results in a function where the peak position is far below the peak top. An empirical approach by Avdeev *et al.* (2007) simply requires tables to be established from individual peak fits to a standard material powder pattern for the values of α, β and TOF in place of the expressions given in equations (3.3.20) and (3.3.21); this establishes the G_λ and G_I contributions to the TOF line shape. More recently, some simple extensions (Toby & Von Dreele, 2013) to the empirical functions [equations (3.3.22) and (3.3.23)] appear to better cover the deviations arising from the enhanced epithermal contribution to the cold moderator spectrum:

$$\mathrm{TOF} = Cd + Ad^2 + B/d + Z, \tag{3.3.22}$$

$$\alpha = \frac{\alpha_1}{d}; \quad \beta = \beta_0 + \frac{\beta_1}{d^4} + \frac{\beta_2}{d^2}; \quad \sigma = \sigma_0 + \sigma_1 d^2 + \sigma_2 d^4 + \frac{\sigma_3}{d^2}. \tag{3.3.23}$$

3.3.4. Peak profiles for X-ray energy-dispersive experiments

In an X-ray dispersive powder diffraction experiment, a detector with good energy-discrimination capability is placed at a fixed scattering angle while the sample is illuminated by a 'white' beam of radiation. The detector response is binned into discrete energies by a multichannel analyser (MCA) (Glazer *et al.*, 1978). Typically these instruments display peaks that are purely Gaussian in shape with quite low resolution ($\Delta E/E \simeq 1\%$) and have widths that are proportional to the energy:

$$\Gamma_G = UE + W. \tag{3.3.24}$$

This is most useful for experiments with very limited angular access (*e.g.* high-pressure multi-anvil setups, as described in Chapter 2.7) using synchrotron radiation and can give very high data collection rates on very small samples. Glazer *et al.* (1978) showed that simple crystal structures can be modelled with the Rietveld technique after suitable corrections to account for the variation in source intensity, detector response and sample absorption effects. Otto (1997) expanded the peak-profile description to include possible sample-broadening effects *via* a Voigt profile; this extended the expression in equation (3.3.24) by adding a second-order term in energy and allowed extraction of

size and microstrain sample-broadening effects in cases where these were large.

A related alternative technique (Wang *et al.*, 2004) collects multiple energy-dispersive powder patterns over a narrow and coarse angular step scan; this is easily done in a typical multi-anvil high-pressure setup. The array of spectra are binned as multiple angle-dispersive patterns which are then combined into a single refinement; the complex corrections required for pure energy-dispersive patterns reduce to refinable scaling factors. Typically a scan over 10° 2θ with 0.1–0.2° steps suffices to give suitable data; binning into $\Delta E/E \simeq 20\%$ energy bands gives data that are used in a conventional multiple-data-set Rietveld refinement.

3.3.5. Sample broadening

Very often, particularly for synchrotron-radiation experiments, the powder diffraction peak profile is dominated by broadening effects from the sample, *e.g.*

$$P(\Delta) = G_\lambda * G_I * G_S \simeq G_S. \tag{3.3.25}$$

For the cases considered here, the focus will be on sample-broadening models that allow improved fits within the context of a Rietveld refinement; a more detailed treatment aimed at extracting sample characteristics (*e.g.* crystallite size distributions) is covered in Chapter 5.1.

Two mechanisms for sample broadening are considered here: crystallite size and 'microstrain' broadening; each will be discussed in turn.

3.3.5.1. *Crystallite size broadening*

The reciprocal space associated with an ideal large crystal will consist of a periodic array of infinitely sharp δ functions, one for each of the structure factors, as expected from the Fourier transform of the essentially infinite and periodic crystal lattice. For real crystals, this limit is reached for crystal dimensions exceeding *circa* 10 μm. The Fourier transform of a crystal lattice that is smaller than this will show a profile that follows the form described by the $\mathrm{sinc}(x) = \sin(\pi x)/\pi x$ function. Any dispersion in the crystal sizes in a powder sample will smear this into a form intermediate between a Gaussian and a Lorentzian, which is well described by either a Voigt [equation (3.3.9)], a pseudo-Voigt [equation (3.3.8)] or the less-useful Pearson VII [equation (3.3.7)] function. The physical process used to form the powder will influence the details of the size distribution; usually this will approximate a log-normal distribution and the resulting peak-shape contribution from crystallite size effects will be largely Lorentzian with a width Γ_{SL}. Predominantly Gaussian size broadening can only occur if the size distribution is very tightly monodisperse. Then, for isotropic crystal dimensions this broadening is uniformly the same everywhere in reciprocal space; *e.g.* Δd^* = constant $\simeq 1/p$, where p is the crystallite size. Transformation *via* Bragg's law to the typical measurement of a powder pattern as a function of 2θ gives this Lorentzian width as

$$\Gamma_{pL} = \frac{180}{\pi}\frac{K\lambda}{p\cos\theta} \tag{3.3.26}$$

expressed in degrees and the Scherrer constant, K, which depends on the shape of the crystallites; *e.g.* K = 1 for spheres, 0.89 for cubes *etc.* (see Table 5.1.1 in Chapter 5.1). A similar expression for the crystallite size from a neutron TOF experiment is

$$\Gamma_{pL} = \frac{CK}{p}, \tag{3.3.27}$$

where C is defined by equation (3.3.21). In some cases the crystallites have anisotropic shapes (*e.g.* plates or needles), in which case the peak broadening will be dependent on the respective direction in reciprocal space for each reflection. Many Rietveld refinement programs implement various models for this anisotropy.

3.3.5.2. *Microstrain broadening*

The existence of imperfections (*e.g.* deformation faults) within the crystal lattice produces local distortions of the lattice and thus a broadening of the points in reciprocal space. To a first approximation these points are broadened proportionally to their distance from the origin, *e.g.* $\Delta d^*/d^* = \Delta d/d \simeq$ constant.

As for crystallite size, there is normally dispersion in the density of defects and thus the peak shape will be intermediate between a Gaussian and a Lorentzian form, and it is well described by the Voigt, pseudo-Voigt or Pearson VII functions. Usually, the Lorentzian form dominates this type of broadening and it is the most common form of sample broadening in powder diffraction. It usually arises because of defects introduced during sample preparation (especially during grinding). The Lorentzian width contribution from microstrain broadening is

$$\Gamma_{sL} = \frac{180}{\pi} s\tan\theta, \tag{3.3.28}$$

where s is the dimensionless microstrain; it is frequently multiplied by 10^6. A similar expression for neutron TOF is

$$\Gamma_{sL} = Csd, \tag{3.3.29}$$

where C is defined by equation (3.3.21).

In many cases, the microstrain broadening is not isotropic; presumably this is a consequence of the interaction between the defects and the elastic properties of the crystals. A phenomenological description of these effects by Popa (1998) and Stephens (1999) is obtained by considering the variance of

$$\frac{1}{d^2} = M_{hkl} = \alpha_1 h^2 + \alpha_2 k^2 + \alpha_3 l^2 + \alpha_4 kl + \alpha_5 hl + \alpha_6 hk \tag{3.3.30}$$

with respect to each of the coefficients α_i.

$$\Gamma_{sL}^2 = \sum_{i,j} S_{ij}\frac{\partial M}{\partial\alpha_i}\frac{\partial M}{\partial\alpha_j} \tag{3.3.31}$$

where

$$\frac{\partial M}{\partial\alpha_i}\frac{\partial M}{\partial\alpha_j} = \begin{bmatrix} h^4 & h^2k^2 & h^2l^2 & h^2kl & h^3l & h^3k \\ h^2k^2 & k^4 & k^2l^2 & k^3l & hk^2l & hk^3 \\ h^2l^2 & k^2l^2 & l^4 & kl^3 & hl^3 & hkl^2 \\ h^2kl & k^3l & kl^3 & k^2l^2 & hkl^2 & hk^2l \\ h^3l & hk^2l & hl^3 & hkl^2 & h^2l^2 & h^2kl \\ h^3k & hk^3 & hkl^2 & hk^2l & h^2kl & h^2k^2 \end{bmatrix}. \tag{3.3.32}$$

Examination of this sum for the triclinic case collects terms to give

$$\begin{aligned}\Gamma_{sL}^2 = {} & S_{400}h^4 + S_{040}k^4 + S_{004}l^4 + 3(S_{220}h^2k^2 + S_{202}h^2l^2 + S_{022}k^2l^2) \\ & + 2(S_{310}h^3k + S_{103}hl^3 + S_{031}k^3l + S_{130}hk^3 + S_{301}h^3l + S_{013}kl^3) \\ & + 4(S_{211}h^2kl + S_{121}hk^2l + S_{112}hkl^2)\end{aligned} \tag{3.3.33}$$

with 15 coefficients S_{hkl}. The subscript hkl in S_{hkl} refers to the powers used for h, k, l in equations (3.3.33)–(3.3.44).